

Postsynaptic Ca^{2+} Influx Mediated by Three Different Pathways during Synaptic Transmission at a Calyx-Type Synapse

Johann H. Bollmann, Fritjof Helmchen, J. Gerard G. Borst, and Bert Sakmann

Abteilung Zellphysiologie, Max-Planck-Institut für medizinische Forschung, D-69120 Heidelberg, Germany

Whole-cell recordings and Ca^{2+} flux measurements were made at a giant calyx-type synapse in rat brainstem slices to determine the contribution of glutamate receptor (GluR) channels and voltage-dependent Ca^{2+} channels (VDCCs) to postsynaptic Ca^{2+} influx during synaptic transmission. A single presynaptic action potential (AP) evoked an EPSP, followed by a single AP. The EPSP-AP sequence caused a postsynaptic Ca^{2+} influx of $\sim 3.0 \text{ pC}$, primarily through VDCCs ($\sim 70\%$) and NMDA-type (up to 30%) channels but also through AMPA-type ($<5\%$) GluR channels. At -80 mV , the fractional Ca^{2+} current (P_f) mediated by AMPA receptor (AMPAR) and NMDA receptor (NMDAR) channels was 1.3 and $11\text{--}12\%$, respectively. Simulations of the time course of Ca^{2+} influx through GluR channels suggested

Inflow of Ca^{2+} into neurons serves many functions. Increases in presynaptic Ca^{2+} concentration trigger neurotransmitter release and control different forms of short-term synaptic plasticity (Katz, 1969; Zucker, 1994). Ca^{2+} entry into the postsynaptic cell controls dendritic excitability (Kennedy, 1989), both increases and decreases in synaptic efficacy (Bliss and Collingridge, 1993), and gene expression (Gallin and Greenberg, 1995; Bito et al., 1997).

The postsynaptic Ca^{2+} influx at excitatory glutamatergic synapses occurs via several pathways. First, glutamate receptor (GluR) channels are Ca^{2+} -permeable. Their permeability depends on the receptor subtype and subunit composition (Burnashev, 1996). The permeability of Ca^{2+} relative to monovalent cations can be derived from reversal potential measurements under bi-ionic conditions. A more direct measure of Ca^{2+} influx is the fractional Ca^{2+} current (P_f), which is the ratio of the Ca^{2+} charge to the charge carried by all permeant cations. P_f values have been obtained in simultaneous measurements of whole-cell currents and fluorescence changes of the Ca^{2+} indicator fura-2 (Schneggenburger et al., 1993; Neher, 1995) during nonsynaptic application of GluR agonists. Under these conditions, NMDA-type GluR channels are more permeable to Ca^{2+} than AMPA-type GluR channels (Schneggenburger et al., 1993; Burnashev et al., 1995; Garaschuk et al., 1996). A second pathway for Ca^{2+} entry is voltage-dependent Ca^{2+} channels (VDCCs), which may

that the small contribution of AMPAR channels occurred only during the first few milliseconds of an EPSP, whereas influx through NMDAR channels dominated later. The NMDAR-mediated Ca^{2+} influx was localized in regions covered by the presynaptic terminal, whereas the Ca^{2+} influx mediated by VDCCs was more homogeneously distributed. Because of the temporal and spatial differences, calcium ions entering through the three different pathways are likely to activate different intracellular targets in the postsynaptic cell.

Key words: action potential; fura-2; fractional Ca^{2+} current; postsynaptic Ca^{2+} influx; medial nucleus of the trapezoid body; calyx of Held; glutamate receptors; Ca^{2+} channels; Ca^{2+} imaging

be opened during postsynaptic depolarizations. Ca^{2+} enters through low-threshold VDCCs in dendrites during subthreshold EPSPs (Markram and Sakmann, 1994; Magee et al., 1995), and evidence has accumulated for the presence of high-threshold VDCCs in dendritic shafts and spines (Denk et al., 1996). A third possible source of postsynaptic increases of the cytoplasmic intracellular Ca^{2+} concentration ($[\text{Ca}^{2+}]_i$) is the release of Ca^{2+} from intracellular stores after synaptic activation (Eilers and Konnerth, 1997).

Little is known, however, about the amount of Ca^{2+} entering the postsynaptic cell at a single synapse, the relative contribution of the different pathways during synaptic transmission, and the localization of postsynaptic Ca^{2+} entry. We addressed these questions in a giant axosomatic synapse located in the medial nucleus of the trapezoid body (MNTB) in rat brainstem slices and measured postsynaptic Ca^{2+} influx using whole-cell recordings combined with fura-2 fluorescence measurements.

The MNTB serves as an inverting relay in the auditory pathway (Helfert and Aschoff, 1997). It receives input from the contralateral anteroventral cochlear nucleus and projects to the ipsilateral lateral superior olive. Each of the MNTB principal neurons is excited by a single large presynaptic terminal, and each presynaptic action potential (AP) elicits a single EPSP and postsynaptic AP (Guinan and Li, 1990; Banks and Smith, 1992; Forsythe and Barnes-Davies, 1993; Borst et al., 1995). Taking advantage of the large size of the synaptic currents, we quantified the contribution of VDCCs and of two classes of GluR channels to the Ca^{2+} influx during normal synaptic transmission. In contrast to earlier studies, we directly measured the P_f values of AMPA receptor (AMPAR) and NMDA receptor (NMDAR) channels during synaptic activation, and we investigated, using imaging techniques, the subcellular location of the Ca^{2+} entry via the different pathways.

Received July 29, 1998; revised Sept. 28, 1998; accepted Oct. 5, 1998.

J.G.G.B. was supported by a Training and Mobility of Researchers fellowship. We thank M. Kaiser for technical assistance, N. Burnashev for critical comments on this manuscript, and L. P. Wollmuth for helpful discussions.

Correspondence should be addressed to Dr. Bert Sakmann, Abteilung Zellphysiologie, Max-Planck-Institut für medizinische Forschung, Jahnstrasse 29, D-69120 Heidelberg, Germany.

Dr. Helmchen's present address: Biological Computation Research Department, Bell Laboratories, Lucent Technologies, 600 Mountain Avenue, Murray Hill, NJ 07974.

Copyright © 1998 Society for Neuroscience 0270-6474/98/1810409-11\$05.00/0

MATERIALS AND METHODS

Whole-cell recordings and solutions. Transverse brainstem slices (200- μm -thick) were cut from 8- to 10-d-old Wistar rats using a Vibratome (Campden Instruments, Loughborough, England). Slices were incubated for 30 min at 37°C and maintained at room temperature (22–24°C) thereafter. The extracellular solution contained (in mM): 125 NaCl, 2.5 KCl, 1 MgCl₂, 2 CaCl₂, 25 dextrose, 1.25 NaH₂PO₄, 0.4 ascorbic acid, 3 myo-inositol, 2 sodium pyruvate, and 25 NaHCO₃, pH 7.4 when bubbled with carbogen (95% O₂ and 5% CO₂). During slice preparation, 0.1 mM CaCl₂ and 3 mM MgCl₂ were used instead. Slices were mounted on an upright microscope (Axioskop FS; Zeiss, Oberkochen, Germany) and continuously superfused at 1–3 ml/min. All experiments were done at room temperature.

MNTB principal neurons were visually identified using an infrared illumination system (Luigs & Neumann, Ratingen, Germany). They were afferently stimulated with a bipolar electrode (5–30 V, 10–40 μsec) placed in the trapezoid body at the mid-line (Borst et al., 1995). Whole-cell recordings from principal neurons were made with thick-walled borosilicate glass pipettes (2–3 M Ω) using an Axopatch 200B amplifier (Axon Instruments, Foster City, CA). Currents and voltages were filtered at 3 kHz (8-pole Bessel filter; Frequency Devices, Haverhill, MA) and sampled at 20 kHz with a 16-bit analog-to-digital converter (ITC-16; Instrutech, Great Neck, NY) interfaced to a PowerPC using Pulse Control version 4.6 (Herrington and Bookman, 1994). In voltage-clamp experiments, the uncompensated series resistance was <24 M Ω , and series resistance compensation was at least 85%. Potentials were corrected for a –11 mV junction potential between the extracellular and pipette solution. The fast current-clamp mode of the Axopatch 200B was used for voltage recordings, allowing reliable recording of APs (Magistretti et al., 1996). During current injections, the bridge was balanced. The interval between APs was typically 1 min.

The pipette solution contained (in mM): 115 potassium gluconate, 20 KCl, 10 disodium phosphocreatine, 4 MgATP, 0.3 GTP, and 10 HEPES, pH 7.2 adjusted with KOH. Spermine (0.1 mM) was added to the solution to prevent alteration of AMPAR current rectification (Koh et al., 1995b). Different concentrations of fura-2 (Molecular Probes, Portland, OR) were added to the solution as noted. Current–voltage (*I*–*V*) relationships of GluR-mediated currents were measured with K⁺ replaced by Cs⁺ in the intracellular solution. Ca²⁺ currents were isolated as described by Borst et al. (1995). To study AMPAR channels in isolation, 50 μM D-(–)-2-amino-5-phosphonopentanoic acid (D-APV) (Tocris Cookson, Bristol, UK) was added to the bath. In a few experiments, desensitization of AMPAR was minimized by cyclothiazide (50–100 μM ; Tocris). NMDAR channels were pharmacologically isolated with 10 μM 6-nitro-7-sulfamoylbenzo[f]quinoxaline-2,3-dione (NBQX) (Tocris). Current-clamp recordings were performed in the presence of 10 μM extracellular glycine to saturate the glycine binding site of the NMDAR (Wilcox et al., 1996), although in three control experiments there was no rundown of NMDAR-mediated currents for up to 90 min without glycine in the extracellular solution and no effect of adding 10 μM glycine. Glycine receptors were blocked by 10 μM strychnine.

Ca²⁺ flux measurements. Fura-2 fluorescence was measured as described by Helmchen et al. (1997), using a 40× water-immersion objective (0.75 NA; Zeiss) and a 12-bit cooled charge-coupled device (CCD) camera (PXL; Photometrics, Tucson, AZ). Excitation light at 380 nm was attenuated to 4–12% with neutral density filters. Emission light was filtered using a 400 nm dichroic mirror and a 420 nm longpass (TILL Photonics, Munich, Germany). The average fluorescence from a fixed region (80 × 80 pixels) on the frame transfer CCD chip was measured with 57 msec sampling interval. Camera pixels in this region were binned 4 × 5 to reduce noise, staying within the dynamic range of the camera. Binned pixels were averaged off-line. For ratiometric measurements, the fura-2 fluorescence at the Ca²⁺-insensitive excitation wavelength (355 nm) was measured directly before and after each measurement and was interpolated (Helmchen et al., 1997).

Ca²⁺ fluxes were measured using 1 mM fura-2 to overload MNTB neurons with the Ca²⁺ indicator (Schneeggenburger et al., 1993; Neher, 1995). Assuming a single compartment model in which the competition of the indicator (*B*) with a pool of rapid endogenous buffers (*S*) is considered, the so-called F/Q ratio *f* is given by:

$$f = \frac{\Delta F}{Q_{\text{Ca}}} = f_{\max} \frac{\kappa_B}{1 + \kappa_S + \kappa_B} \quad (1)$$

where ΔF is the fluorescence change, Q_{Ca} is the integral of the Ca²⁺ current, and κ_S and κ_B are the Ca²⁺-binding ratios of the endogenous buffer and the indicator, respectively (Neher and Augustine, 1992). To calculate the exogenous Ca²⁺-binding ratio κ_B , we used the incremental Ca²⁺-binding ratio as defined by Neher and Augustine (1992). Fura-2 overload is reached when κ_B is much larger than κ_S . In this case, *f* approaches f_{\max} , and ΔF is directly proportional to the total Ca²⁺ influx Q_{Ca} . For normalization, all measured fura-2 fluorescence intensities were divided by the average intensity of five fluorescent beads (4.5 μm diameter fluoresbrite BB beads; Polysciences, Warrington, PA), which were measured on each experimental day. Thus, fluorescence decrements (ΔF_{380}) are expressed in “bead units” (BU) (Schneeggenburger et al., 1993). Decrements were determined by taking the difference (evaluated at 400 msec after the stimulus) between the baseline fluorescence and a line fitted to the first 20 data points after the stimulus.

The fractional Ca²⁺ current (*P_f*) specifies the percentage of contribution of Ca²⁺ to the net cation charge (Q_{tot}) through nonselective receptor channels (Schneeggenburger et al., 1993; for review, see Neher, 1995). The time course of the Ca²⁺ charge (Q_{Ca}) was obtained by dividing the fluorescence trace ΔF_{380} by f_{\max} . *P_f* values were determined by scaling Q_{tot} to fit Q_{Ca} within the first 600 msec after the stimulus. Ca²⁺ extrusion was assumed to be negligible during this time window. In a second approach, simulated fluorescence traces, assuming a single rate constant Ca²⁺ extrusion mechanism, were fitted to the entire fluorescence trace according to Schneeggenburger et al. (1993), their Equation 8.

Current waveform injections. In current-clamp recordings, injection of current waveforms was used to generate membrane potential changes similar to those evoked by synaptically activated currents through GluR channels. Rather than using a dynamic clamp to perform conductance injection (Robinson and Kawai, 1993; Sharp et al., 1993), we used a more empirical approach to find a current waveform that would mimic the effect of the synaptic currents. The injected current (*I_{inj}*) consisted of three components:

$$I_{\text{inj}}(t) = I_{\text{AMPA}} A(t) + I_{\text{NMDA}} B(t) - I_{\text{shunt}} C(t) \quad (2)$$

The time course of the AMPAR-mediated current [*A*(*t*)] was modeled as an exponentially rising and biexponentially falling waveform [τ_{rise} , 100 μsec ; τ_{fast} , 1–1.2 msec (98% of amplitude); τ_{slow} , 14 msec] (Borst et al., 1995). A similar waveform but with slower kinetics was used for the NMDAR-mediated component [*B*(*t*)] [τ_{rise} , 2–2.6 msec; τ_{fast} , 44 msec (65%); τ_{slow} , 147 msec] (Barnes-Davies and Forsythe, 1995). These temporal functions represent the conductance changes of the GluR channels, which are proportional to the EPSCs in voltage clamp. In current clamp, however, the driving force for the synaptic currents changes and even reverses sign during the AP. Thus, the synaptic conductance increase of GluR channels shunts other ionic currents, e.g., Na⁺ currents, which leads to a reduction of the AP amplitude. To account for these effects, we empirically subtracted a Gaussian-shaped term [*C*(*t*)] during the rapid phase of the AP (mean, 0.55–0.9 msec; SD, 0.16–0.2 msec). The ranges of amplitudes used for the three current components were I_{AMPA} , 2.4–4 nA, I_{NMDA} , 8–160 pA, and I_{shunt} , 0.6–2 nA. The waveform parameters were slightly varied during the experiment, e.g., the current amplitudes and the onset of the Gaussian, to optimize the overlay of the AP evoked by current waveform injection with the afferently stimulated one. The waveforms obtained with this approach resembled currents measured during APs using dynamic clamp of the conductance (Robinson and Kawai, 1993; Reyes et al., 1996). If APs were evoked by afferent stimulation but in the presence of D-APV, only the NMDAR-mediated current component was substituted [*A*(*t*) = *C*(*t*) = 0].

Some rundown was observed in the postsynaptic Ca²⁺ influx, estimated to be on average 9%/10 min. To minimize the contribution of rundown, Ca²⁺ influx was measured between 10 and 35 min after break-in. In experiments in which the effect of D-APV was tested, the Ca²⁺ influx evoked by current waveform injection had to be constant within 25% throughout the experiment to be accepted.

Simulation of Ca²⁺ influx through GluR channels. *I*–*V* relationships for peak currents through AMPAR channels were fitted with fifth-order polynomials. The voltage-dependent Mg²⁺ block of NMDAR channels was modeled using Woodhull's theory (Woodhull, 1973):

$$I(V) = g_{\text{NMDA}} (V - E_{\text{rev}}) / [1 + [\text{Mg}^{2+}]_0 \exp(-\delta z F V / RT) / K_0] \quad (3)$$

where g_{NMDA} denotes the peak conductance, assuming a linear *I*–*V* relationship in the absence of Mg²⁺, E_{rev} is the reversal potential of the

synaptic conductance, $[\text{Mg}^{2+}]_o$ is the external Mg^{2+} concentration, K_0 represents the IC_{50} at 0 mV, δ is the apparent electrical distance of the Mg^{2+} binding site from the outside of the membrane, z is the valence of Mg^{2+} , and F , R , and T have their usual thermodynamic meanings. The voltage dependence of the P_f was modeled according to the Goldman–Hodgkin–Katz (GHK) current equation (Schneggenburger et al., 1993; Burnashev et al., 1995; Koh et al., 1995a), assuming the internal Ca^{2+} concentration to be zero:

$$P_f(V) = \left\{ 1 + \frac{1}{4} \frac{P_M}{P_{\text{Ca}}} \frac{[M]}{[\text{Ca}^{2+}]_o} [1 - \exp(2 FV/RT)] \right\}^{-1} \quad (4)$$

where P_{Ca}/P_M denotes the relative permeability to Ca^{2+} compared with the monovalent cations, which were assumed to all have the same permeability. $[M]$ represents the total activity of monovalent cations obtained by multiplying a concentration of 155 mM with an activity coefficient of 0.76 on both sides of the membrane. Similarly, the external Ca^{2+} concentration of 2 mM was multiplied with an activity coefficient of 0.58 (Spruston et al., 1995). P_{Ca}/P_M was calculated from the measured P_f values at –80 mV. For AMPAR, P_{Ca}/P_M was 0.33, lower than the value of 1.1 that was obtained in outside-out patches (Geiger et al., 1995). Possible causes for this discrepancy between measured and calculated P_{Ca}/P_M values are discussed by Burnashev et al. (1995).

To simulate the Ca^{2+} influx through GluR channels during a suprathreshold EPSP, the Ca^{2+} current through AMPAR and NMDAR channels was calculated for each membrane potential by multiplying the I – V relationship with $P_f(V)$ (see Fig. 6c,f). The reversal potentials of the modeled GluR currents were set equal to the reversal potentials predicted by the assumptions used for Equation 4 (Spruston et al., 1995).

Ca^{2+} imaging. To determine the localization of postsynaptic Ca^{2+} influx, simultaneous presynaptic and postsynaptic recordings from MNTB synapses were performed (Borst et al., 1995). Presynaptic terminals were loaded with 0.4–1 mM MagFura-2 and principal neurons with 0.4–1 mM Oregon Green 488 BAPTA-5N (OGB-5N) (both from Molecular Probes). Using a 500 nm dichroic mirror and a 510 nm longpass filter, the fluorescence of the two dyes was separated by exciting at 380 and 488 nm, respectively, without the need to change filters. The presynaptic pipette solution contained K^+ when afferent stimulation was used, whereas the postsynaptic solution contained Cs^+ to block K^+ channels. A 60× water-immersion objective (0.9 NA; Olympus Optical, Tokyo, Japan) was used in conjunction with a fast 12-bit CCD camera (Borst et al., 1995). Image series of the postsynaptic neuron were acquired at 30 Hz from a subarray of 110×110 pixels containing the MNTB principal neuron. Images were smoothed with a 3×3 pixel Gaussian filter. Prestimulus images were averaged to obtain a basal fluorescence image, which was subtracted from all images to obtain difference images (ΔF). Assuming spatially homogeneous Ca^{2+} -binding ratios and in the absence of buffer saturation, these difference images represent the accumulation and spread of Ca^{2+} , because ΔF is proportional to Q_{Ca} under these conditions (Eq. 1).

RESULTS

Fura-2 overload in MNTB principal neurons

Postsynaptic Ca^{2+} fluxes in MNTB principal neurons were studied using the fura-2 overload technique. If applied in sufficiently high concentrations, fura-2 outcompetes endogenous Ca^{2+} buffers and reports Ca^{2+} fluxes rather than Ca^{2+} concentrations (Neher, 1995). To define conditions for fura-2 overload in MNTB neurons, visually identified neurons were loaded with different concentrations of fura-2 via whole-cell patch pipettes (Fig. 1a–c). The loading time course could be described by a single exponential function with a time constant of 104 ± 13 sec (mean \pm SEM; $n = 13$) (fit not shown). During loading of a cell, Ca^{2+} currents were elicited by brief depolarizing voltage steps, resulting in transient fura-2 fluorescence decrements at an excitation wavelength of 380 nm (ΔF_{380}). As the intracellular fura-2 concentration rose from 0.05 to 0.5 mM, Ca^{2+} currents of similar size evoked ΔF_{380} of increasing amplitudes (Fig. 1d). At fura-2 concentrations larger than 0.5 mM (corresponding to a fura-2 Ca^{2+} -binding ratio $\kappa_B > 1000$), no further changes in the ratio of ΔF_{380} over the Ca^{2+} current integral (F/Q ratio, see Materials

and Methods) were resolved (Fig. 1e). Fluorescence changes were also ratiometrically converted to changes in intracellular free Ca^{2+} concentration ($[\text{Ca}^{2+}]_i$). With increasing fura-2 concentration, the amplitude of $[\text{Ca}^{2+}]_i$ transients decreased, whereas the decay to the resting level was prolonged (Fig. 1d). After loading with 1 mM fura-2, $[\text{Ca}^{2+}]_i$ transients had a peak amplitude of 8.4 ± 0.8 nm and decayed with time constants >5 sec ($n = 13$).

These results demonstrate that fura-2 effectively competes with the endogenous Ca^{2+} buffers. At a concentration of 1 mM, fura-2 captured virtually all incoming Ca^{2+} . Therefore, we assumed that ΔF_{380} is proportional to the charge Q_{Ca} under these conditions. The proportionality constant, which is the maximal F/Q ratio f_{max} , was determined by applying depolarizing voltage steps of different duration (5–30 msec) after loading with 1 mM fura-2 and was 15.2 ± 0.6 BU/nC ($n = 12$) (data not shown). To obtain an estimate of the endogenous Ca^{2+} -binding ratio κ_S , we plotted the F/Q ratios of all loading experiments versus the fura-2 Ca^{2+} -binding ratio κ_B (Fig. 1e). A fit of the data according to Equation 1, with f_{max} held constant at the above value, yielded a value of 80–90 for κ_S , indicating that the Ca^{2+} -binding ratio of the endogenous buffers was equivalent to a fura-2 concentration of $<50 \mu\text{M}$. In subsequent experiments, we overloaded MNTB neurons with 1 mM fura-2 to measure postsynaptic Ca^{2+} influx during synaptic transmission.

Ca^{2+} influx during a single suprathreshold EPSP

At the MNTB synapse, a single presynaptic AP elicits large postsynaptic currents. They generate an EPSP that initiates a single postsynaptic AP. After loading MNTB neurons with fura-2, the Ca^{2+} influx during the AP that was evoked by afferent stimulation could be quantified (Fig. 2a). Evoked EPSPs rapidly (~ 0.5 msec) reached threshold, initiating an AP that had an amplitude of 96 ± 2 mV and a half-width of 1.01 ± 0.05 msec ($n = 18$; Fig. 2b, left). The AP was followed by a slow depolarizing afterpotential. Ten milliseconds after stimulation, its amplitude was 12 ± 2 mV above the resting membrane potential of -71 ± 1 mV. It decayed half-maximally in 43 ± 7 msec (Fig. 2c). The afterpotential was also present at low fura-2 concentrations (10 – $50 \mu\text{M}$; $n = 5$) (data not shown), indicating that it was not caused by the overload method. The postsynaptic AP was accompanied by large fura-2 fluorescence decrements, corresponding to an average Ca^{2+} charge of 3.0 ± 0.4 pC (Fig. 2a,d). Thus, approximately 9×10^6 calcium ions entered a principal neuron during a single afferently evoked postsynaptic AP. We next evaluated the relative contributions of VDCCs and NMDAR and AMPAR channels to the total Ca^{2+} influx.

Contribution of VDCCs to Ca^{2+} influx during a suprathreshold EPSP

During an afferently evoked AP, Ca^{2+} enters the postsynaptic cell via both GluR channels and VDCCs. To dissect the relative contribution of these pathways, we evoked APs by current injection via the patch pipette. These APs will selectively activate VDCCs. Pulse-like current injections evoked APs that had larger amplitudes (100 ± 1 mV) and shorter half-widths (0.87 ± 0.04 msec) when compared with afferently evoked APs (Fig. 2b, middle). They lacked the slow afterpotential. Instead, they were followed by an afterhyperpolarization (Fig. 2c). The associated ΔF_{380} corresponded to 1.7 ± 0.2 pC ($n = 9$), significantly less than during a synaptically evoked AP. Because Ca^{2+} currents through VDCCs critically depend on the shape of the AP, we used current waveform injections to elicit APs whose shape resembled synap-

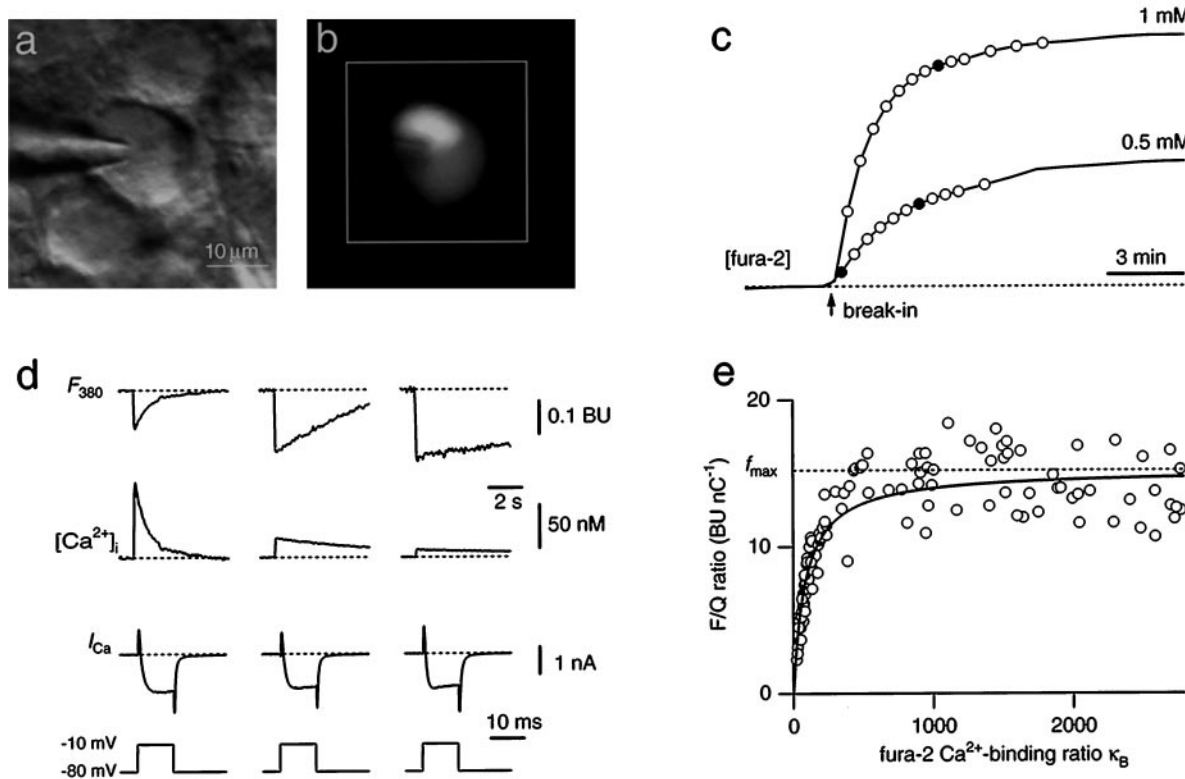


Figure 1. Combined whole-cell recordings and fura-2 measurements from MNTB neurons. *a*, Infrared video image of a MNTB principal neuron with a whole-cell patch pipette. *b*, Fluorescence image of the same neuron filled with 1 mM fura-2. The white square indicates the region on the CCD chip from which average fluorescence signals were measured. *c*, Two examples of loading an MNTB neuron with 0.5 and 1 mM fura-2, respectively. The fura-2 concentration was monitored at the Ca^{2+} -insensitive excitation wavelength (solid lines). It was assumed that the concentration of fura-2 in the pipette and the cell were the same when the fluorescence intensity reached a plateau level. During fura-2 loading, Ca^{2+} currents were evoked by 10 msec depolarizing voltage steps from -80 to -10 mV in 30–60 sec intervals (circles). *d*, Examples of fluorescence decrements at 380 nm excitation (F_{380}) evoked by brief Ca^{2+} currents (I_{Ca}). Traces are from the loading experiments shown in *c* at the times indicated by the filled circles. Assuming equilibrium with the patch pipette concentration when the fluorescence reached a plateau level, the intracellular fura-2 concentration was 60 (left), 330 (middle), and 880 μM (right). Fluorescence decrements are expressed in bead units and were ratiometrically converted to changes in Ca^{2+} concentration ($[Ca^{2+}]_i$). Note differences in time scale. *e*, Summary plot of the dependence of the F/Q ratio on the fura-2 Ca^{2+} -binding ratio κ_B . Data points are from 13 loading experiments using different fura-2 pipette concentrations ranging between 50 μM and 1 mM. A curve according to Equation 1 was fitted to the data with f_{\max} held constant at 15.2 BU/nC and κ_S as the free parameter in the fitting procedure.

tically evoked APs more closely. The waveform of the current injected was based on the time course of the conductance changes of the AMPAR and NMDAR channels and their shunting effect on the amplitude of the AP (see Materials and Methods). APs evoked by current waveform injections closely matched those evoked by afferent stimulation (Fig. 2*b*, right). Their amplitude was 96 ± 2 mV, and their half-width was 1.04 ± 0.04 msec ($n = 18$). They also displayed the slow afterpotential (Fig. 2*c*). In this case, the evoked ΔF_{380} corresponded to a Ca^{2+} charge of 2.0 ± 0.3 pC (Fig. 2*d*). The Ca^{2+} influx evoked by current waveform injections was $70 \pm 3\%$ of the Ca^{2+} influx evoked by afferent stimulation in the same cells ($n = 18$). Thus, ~70% of the total postsynaptic Ca^{2+} influx during a suprathreshold EPSP was mediated by VDCCs. This suggests that the remaining 30% originated from GluR channels.

Contribution of NMDAR channels to the Ca^{2+} influx during a suprathreshold EPSP

Postsynaptic currents in MNTB principal neurons are mediated by both AMPAR and NMDAR channels (Forsythe and Barnes-Davies, 1993). To determine the contribution of NMDAR channels to the Ca^{2+} influx during a synaptically evoked AP, we compared the postsynaptic Ca^{2+} influx during a synaptically

evoked AP before and after blocking NMDARs with 50 μM D-APV (Fig. 3). After blocking NMDARs, EPSPs still elicited an AP. However, the decay of the slow afterpotential was faster compared with control (Fig. 3*b*). The ΔF_{380} evoked by these suprathreshold EPSPs corresponded to $62 \pm 5\%$ ($n = 5$) of control. To restore the slow time course of the AP, we substituted the blocked NMDAR-mediated current component by postsynaptic current injection (Fig. 3*c*). Under this condition, ΔF_{380} increased to $69 \pm 4\%$ of the influx during the afferently evoked AP in the control period. Because this increase is small, the increase in the depolarizing afterpotential appeared to have little effect on the VDCCs. Because the Ca^{2+} influx during APs evoked by current waveform injections and during synaptically evoked APs with NMDARs blocked was similar, this suggests that NMDAR channels are the dominating pathway for postsynaptic Ca^{2+} influx through GluR channels.

Fractional Ca^{2+} current through NMDAR channels during unitary EPSCs

To further quantify the Ca^{2+} influx through GluR channels during synaptic transmission, we pharmacologically isolated NMDARs and AMPARs and determined the fractional Ca^{2+} currents during EPSCs. NMDAR-mediated EPSCs were

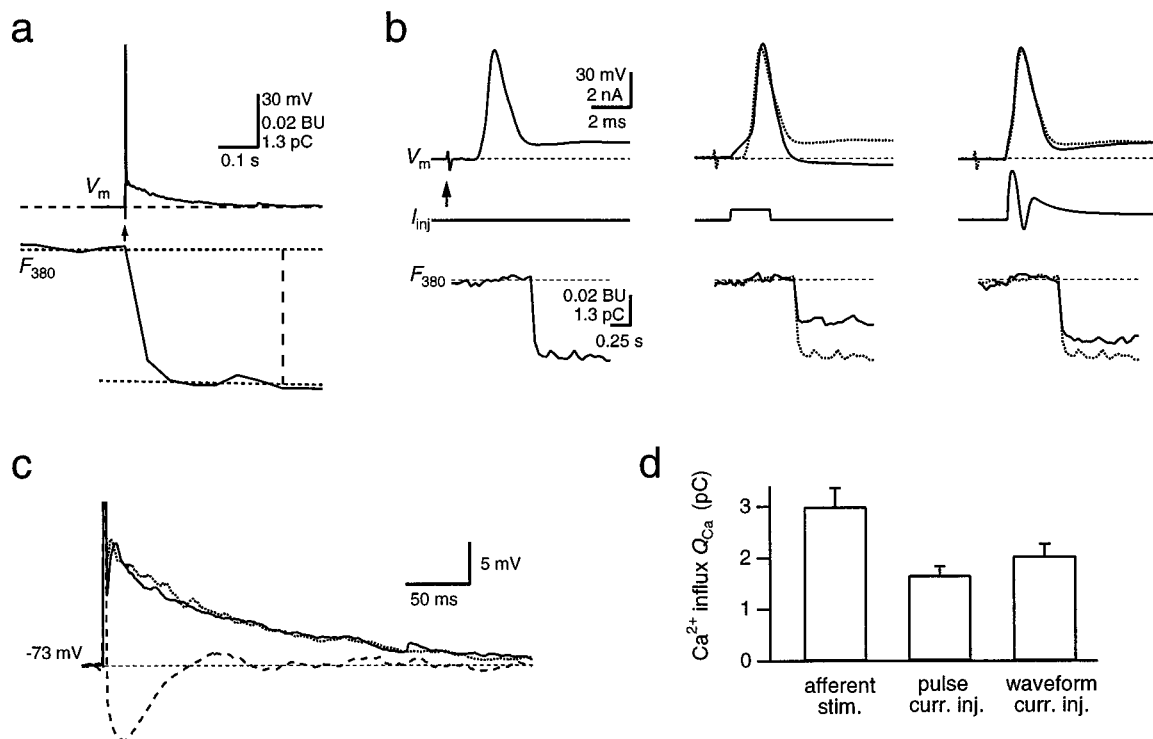


Figure 2. Ca^{2+} influx during a suprathreshold EPSP. *a*, A single postsynaptic AP (top, V_m) in an MNTB principal neuron evoked by afferent stimulation (arrow) displays a fast spike and a slowly decaying afterpotential. The simultaneously recorded fluorescence change (F_{380}) on the same time scale was analyzed ~400 msec after stimulation, as indicated by the vertical dashed line. It was evaluated as the difference between the fluorescence baseline and a straight line fit to the first 20 sample points after the fluorescence decrease. F_{380} is an average of eight sweeps. The decrement is expressed in bead units, as well as in picocoulombs, after conversion to Ca^{2+} charge. *b*, Single APs were evoked by either afferent stimulation (left, arrow), a rectangular current injection pulse (middle; 300 pA for 2 msec), or a waveform current injection (right). Membrane potential (V_m), the injected current (I_{inj}), and the simultaneously measured fluorescence intensity (F_{380}) are shown. Note the different time scale of the fluorescence record. For comparison, the voltage trace and F_{380} measured with the afferent stimulation protocol (dotted traces, middle and right) are overlaid with the traces measured by the current injection protocols. The different stimulation protocols were applied in cyclic order. *c*, Slow afterpotential of the postsynaptic APs evoked by afferent stimulation (dotted trace) and current waveform injection (solid trace) and the pronounced afterhyperpolarization following an AP evoked by a rectangular current pulse (dashed trace) shown on an expanded voltage scale. The peaks of the APs are truncated. *d*, Comparison of the Ca^{2+} charge entering the soma during single APs, which were evoked using the three different stimulation protocols.

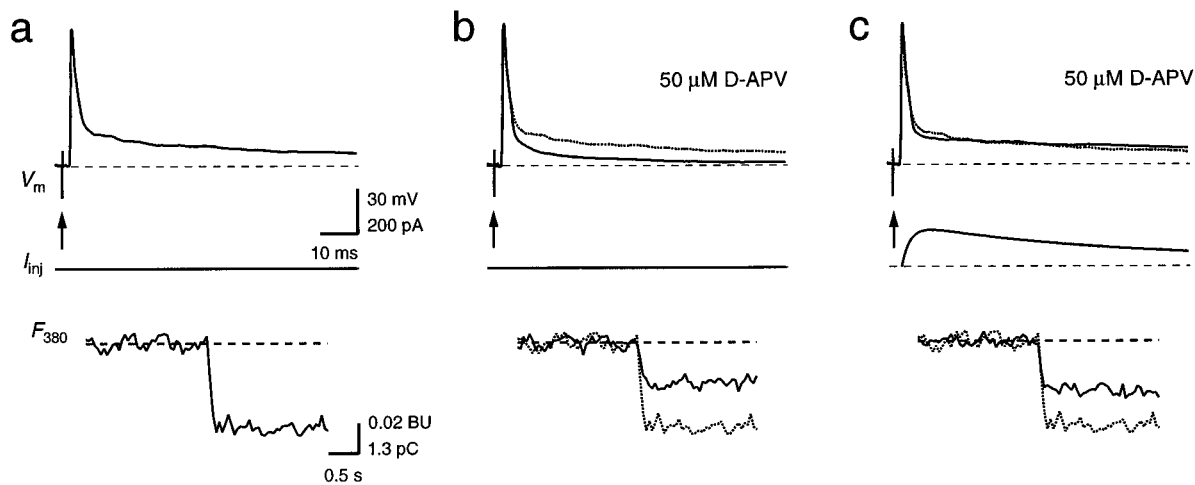


Figure 3. Contribution of NMDAR channels to the Ca^{2+} influx during a suprathreshold EPSP. Single APs in a principal neuron were evoked by afferent stimulation alone (*a*, *b*, arrows) or by a combination of afferent stimulation and current waveform injection (*c*). In *b* and *c*, NMDAR channels were blocked with 50 μM D-APV. The AP (V_m) and the fluorescence intensity (F_{380}) of *a* are shown also in *b* and *c* for comparison (dotted traces). ΔF_{380} in *b* and *c* corresponded to 53 and 59%, respectively, of the total ΔF_{380} in control conditions. Note the different time scale of the fluorescence traces. Calibration bars in *a* also apply to *b* and *c*.

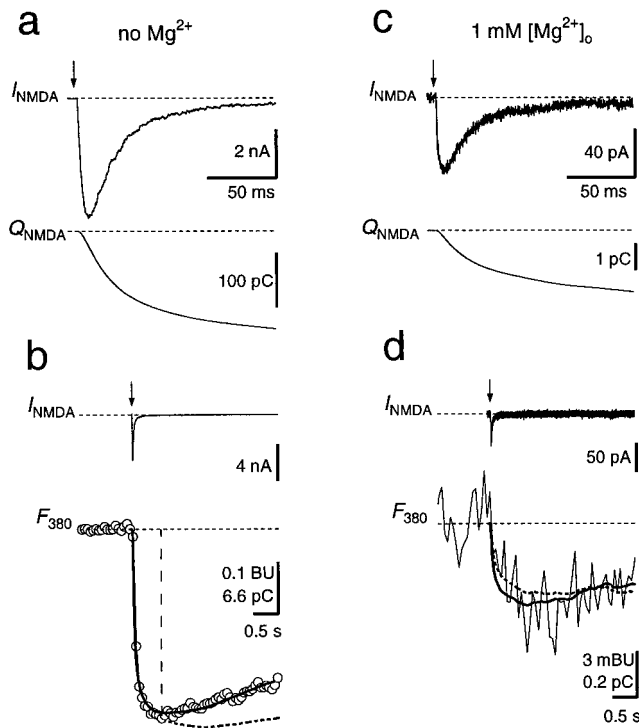


Figure 4. Fractional Ca^{2+} current through NMDAR channels. *a*, A single NMDAR-mediated EPSC (I_{NMDA}) and the current integral (Q_{NMDA}) at a holding potential of -80 mV in Mg^{2+} -free solution. *b*, Same EPSC as in *a* but displayed on a longer time scale, together with the fluorescence trace (F_{380} , open circles) measured simultaneously (1 mM fura-2). F_{380} is given in bead units, as well as in picocoulombs, after conversion to Ca^{2+} charge. P_f was determined by scaling Q_{NMDA} (dashed curve) to fit the time course of F_{380} within the first 0.6 sec after stimulation (vertical dashed line). The scaling factor in this example was 0.111. Alternatively, a curve accounting for Ca^{2+} extrusion (see Materials and Methods) was fitted to the entire fluorescence trace, yielding P_f of 11.7% (solid curve). *c*, NMDAR-mediated EPSC recorded in the same cell as in *a* and *b* but with 1 mM Mg^{2+} in the external solution, at -80 mV. *d*, P_f was 9.7% as determined by scaling of Q_{NMDA} (dashed curve) and 11.5% when a curve was fitted to the entire trace (solid curve). F_{380} and the scaled Q_{NMDA} are averages of 10 sweeps. AMPARs were blocked with 10 μM NBQX. Afferent stimulation is indicated by arrows. Stimulus artifacts were blanked.

measured in principal neurons loaded with fura-2 by blocking AMPARs with NBQX (Fig. 4). In Mg^{2+} -free extracellular solution, EPSCs had amplitudes of several nanoamperes at a holding potential of -80 mV and a relatively slow decay time course (Fig. 4*a,b*). The P_f of the synaptically activated NMDAR channels was determined as the scaling factor between Q_{NMDA} and the decrease in fura-2 fluorescence within a narrow time window (Fig. 4*b*). This yielded a P_f value of $11.4 \pm 0.4\%$ ($n = 9$). Alternatively, P_f was obtained from a fit of the entire time course of ΔF_{380} according to Schneggenburger et al. (1993), their Equation 8, which assumes a Ca^{2+} extrusion mechanism that linearly depends on $[\text{Ca}^{2+}]_i$. The result of this analysis yielded a similar value for P_f ($11.8 \pm 0.4\%$). In six experiments, NMDAR-mediated EPSCs were also measured in the presence of 1 mM $[\text{Mg}^{2+}]_o$. The time course of the EPSCs was not different compared with those in Mg^{2+} -free solution, but their amplitude at -80 mV was reduced ~ 70 -fold, attributable to the voltage-dependent Mg^{2+} block of NMDAR channels (Fig. 4*c,d*). The P_f obtained from the two analysis methods were 11.4 ± 0.9 and $12.4 \pm 2.0\%$, respectively. These values are not significantly

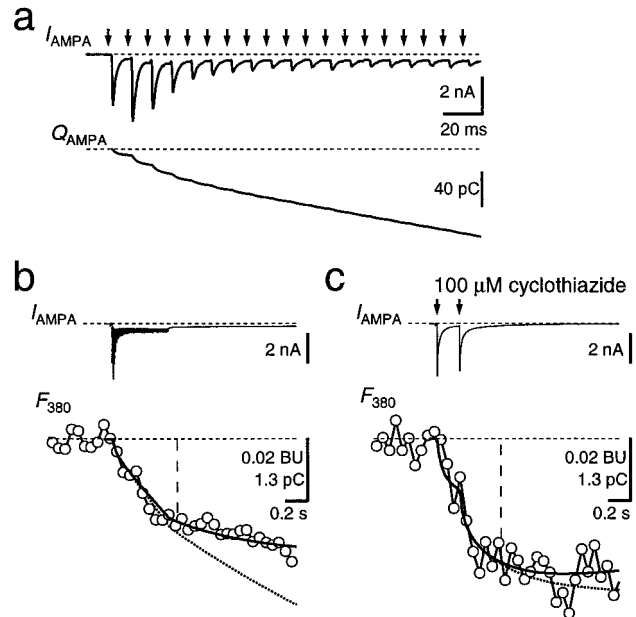


Figure 5. Fractional Ca^{2+} current through AMPAR channels. *a*, Afferent stimulation for 500 msec at 100 Hz (arrows) evoked a train of EPSCs (I_{AMPA}). Holding potential was -80 mV. In this case, the second EPSC facilitated, whereas the subsequent EPSCs displayed strong depression. The current integral (Q_{AMPA}) is shown in the bottom. Stimulus artifacts were blanked. *b*, Same current trace as in *a* shown on a longer time scale (I_{AMPA} , top), together with the associated fluorescence (F_{380} , open circles). The P_f was determined by scaling Q_{AMPA} (bottom, dotted trace) to fit F_{380} within the time window indicated by the vertical line, yielding P_f of 0.83% in this example. A curve fit to the F_{380} trace according to Equation 4 (see Materials and Methods) resulted in P_f of 0.85% (solid curve). Traces are an average of 12 sweeps. *c*, In the presence of cyclothiazide (100 μM) to minimize AMPAR desensitization, two AMPAR-mediated EPSCs (interstimulus interval, 200 msec) evoked a measurable Ca^{2+} influx. Different cell from *a* and *b*. P_f was 1.3% with both analysis methods. Traces are an average of four sweeps.

different from those obtained in Mg^{2+} -free solution ($p > 0.7$; paired t test), confirming that P_f is independent of the Mg^{2+} block (Schneggenburger et al., 1993; Burnashev et al., 1995).

Fractional Ca^{2+} current through AMPAR channels during EPSCs

AMPAR-mediated EPSCs were measured in the presence of D-APV to block NMDAR channels (Fig. 5). These EPSCs had amplitudes of 2–10 nA at -80 mV and a fast time course, as described previously (Forsythe and Barnes-Davies, 1993; Borst et al., 1995). A single EPSC caused a charge entry of 10.4 ± 1.3 pC ($n = 8$) within the first 100 msec after the stimulus but no measurable change in fura-2 fluorescence. High-frequency stimulation was needed to evoke a detectable Ca^{2+} influx (Fig. 5*a,b*). The fractional Ca^{2+} current through AMPAR channels, determined using the two methods described above, was 1.4 ± 0.2 and $1.5 \pm 0.2\%$, respectively ($n = 16$). After repetitive stimulation, a small inward current persisted for several seconds (Fig. 5*b*, I_{AMPA}). This current could be caused by a prolonged presence of glutamate in the synaptic cleft, as has been reported for a different calyx-type synapse (Otis et al., 1996). Addition of the AMPA and kainate receptor blocker NBQX (10 μM) reduced the charge accumulated during a 100 Hz train to $10 \pm 3\%$ ($n = 5$, data not shown). The P_f of the current that was resistant to both D-APV and NBQX ranged between 2 and 6% ($n = 3$), indicating that it was not simply because of an incomplete block of NMDAR.

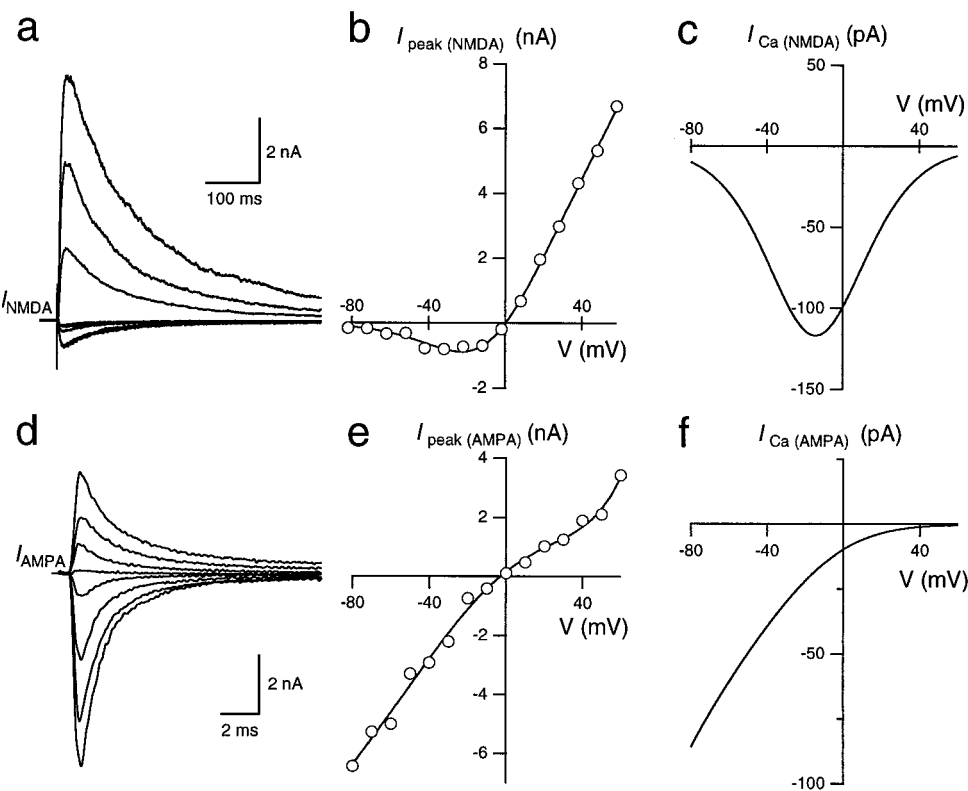


Figure 6. Current–voltage relationships of GluR channels. *a*, NMDAR-mediated EPSCs were measured at holding potentials ranging from -80 to $+60$ mV in 10 mV steps. Every second trace is shown. AMPARs were blocked by NBQX. *b*, The voltage dependence of the peak current through NMDAR channels was fitted according to a Woodhull model (Woodhull, 1973; see Materials and Methods, Eq. 3). *c*, The voltage dependence of the peak Ca^{2+} current through NMDAR channels ($I_{\text{Ca}(\text{NMDA})}$) was calculated by multiplying the I – V shown in *b* with $P_f(V)$, which was obtained from the P_f value measured at -80 mV and calculated for other membrane potentials assuming a GHK model (see Materials and Methods). *d*, AMPAR-mediated EPSCs at holding potentials of -80 to $+60$ mV in 10 mV steps. Every second trace is shown. NMDARs were blocked by D-APV. *e*, The voltage dependence of the peak current through AMPAR channels was fitted using a fifth-order polynom. The filling solution of the whole-cell recording pipette included $100 \mu\text{M}$ spermine. *f*, The voltage dependence of the peak Ca^{2+} current through AMPAR channels ($I_{\text{Ca}(\text{AMPA})}$) was calculated analogous to *c*.

Because of the contribution of the D-APV- and NBQX-resistant current to the Ca^{2+} influx during high-frequency stimulation, we also measured P_f in the presence of cyclothiazide (50 – $100 \mu\text{M}$) to minimize AMPAR desensitization. Under this condition, two to five stimuli at 5 – 10 Hz were already sufficient to detect measurable Ca^{2+} influx (Fig. 5c). The P_f was $1.2 \pm 0.2\%$ with the scaling method and $1.3 \pm 0.2\%$ with the fitting procedure, i.e., $10 \pm 16\%$ lower than the P_f measured in the same cells during high-frequency stimulation in the absence of cyclothiazide. Because cyclothiazide specifically blocks desensitization of AMPAR, this suggests that the Ca^{2+} influx was mediated by AMPAR channels, and thus, we estimate the P_f for AMPAR channels between 1.1 and 1.5% .

From the total charge entry during a single AMPAR-mediated EPSC and with a P_f of 1.4% , it follows that $\sim 0.14 \text{ pC}$ is carried by Ca^{2+} during a single AMPAR-mediated EPSC. This corresponds to $<5\%$ of the total Ca^{2+} influx during a synaptically evoked AP. However, AMPAR channels will contribute even less during an AP, because the driving force for Ca^{2+} decreases during the fast membrane depolarization.

Voltage dependence of the Ca^{2+} influx through GluR channels

The fraction of current through GluR channels that is carried by Ca^{2+} depends on the membrane potential. At depolarized membrane potentials, the fluorometric measurement of Ca^{2+} fluxes through GluR channels is obscured by influx through VDCCs, and extracellular blockers of VDCCs could not be applied, because they would interfere with synaptic transmission (Wu et al., 1998). As an alternative approach based on GHK assumptions (Schneggenburger et al., 1993; Schneggenburger, 1996), we determined the I – V relationships of NMDAR- and AMPAR-mediated EPSCs and calculated the fraction carried by Ca^{2+} using the measured P_f values and Equation 4 (see Materials and

Methods). The I – V relationship for NMDAR-mediated EPSCs had a negative slope conductance for potentials more negative than -20 mV because of the block by extracellular Mg^{2+} (Fig. 6*a,b*). A fit according to Equation 3 yielded a peak conductance g_{NMDA} of 107 nS , a half-maximal blocking concentration $K_{0.5}$ of 2.8 mM , and an electrical distance δ of 0.86 . The calculated Ca^{2+} current $I_{\text{Ca}(\text{NMDA})}$ shows a peak of approximately -120 pA at -15 mV (Fig. 6*c*). This peak results from the opposing effects of the voltage on the relief of the Mg^{2+} block and the reduction in driving force for Ca^{2+} . At positive membrane potentials, Ca^{2+} flux is still inward, although the net total current is flowing outward (Fig. 6*b,c*).

The I – V relationship for AMPAR-mediated EPSCs showed a slight double rectification (Fig. 6*d,e*) because of the voltage-dependent block by polyamines (Koh et al., 1995b). Similar results have been obtained in nucleated patches from the MNTB (A. Rozov and N. Burnashev, personal communication). The calculated Ca^{2+} current $I_{\text{Ca}(\text{AMPA})}$ was -85 pA at -80 mV and monotonically decreased at more positive potentials (Fig. 6*f*). Thus, the voltage dependence of the Ca^{2+} current component differs substantially between NMDAR and AMPAR channels, and the relative contribution of NMDAR channels will increase at depolarized potentials.

Time course of the Ca^{2+} influx through GluR channels during a suprathreshold EPSP

Having measured the fractional Ca^{2+} currents and the time course of the conductance change through GluRs, we could simulate the time course of the Ca^{2+} influx via GluR channels during a suprathreshold EPSP. Based on an average AP time course, the AMPAR- and NMDAR-mediated Ca^{2+} currents were calculated, taking into account the GluR conductance time course and the voltage dependence of the Ca^{2+} influx (Fig. 7).

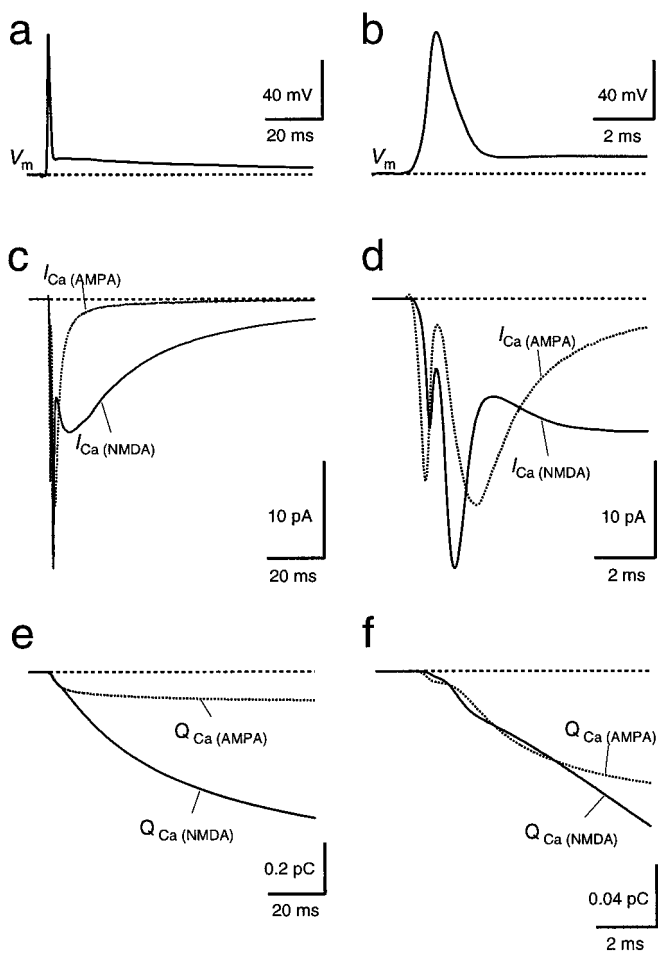


Figure 7. Simulated time course of Ca^{2+} influx through NMDAR and AMPAR channels during a suprathreshold EPSP. *a, b*, The time course of Ca^{2+} influx through AMPAR and NMDAR channels was calculated using an average of postsynaptic APs evoked by afferent stimulation from 18 cells as a voltage template (V_m). The AP is shown in *a* and on an expanded time scale in *b*. *c, d*, The simulated Ca^{2+} currents through AMPAR channels ($I_{\text{Ca}(\text{AMPA})}$, dotted line) and through NMDAR channels ($I_{\text{Ca}(\text{NMDA})}$, solid line) are shown in *c* and on an expanded time scale in *d*. The Ca^{2+} current traces were calculated using the Ca^{2+} $I-V$ (Fig. 6c,f) to obtain the peak Ca^{2+} current for each point of the voltage template. Then, the resulting Ca^{2+} current traces were scaled by the normalized conductance time course of GluR channels as determined from AMPAR- and NMDAR-mediated EPSCs. Integration of the respective Ca^{2+} current traces yielded the time course of Ca^{2+} charge (*e* and *f*, $Q_{\text{Ca}(\text{AMPA})}$, $Q_{\text{Ca}(\text{NMDA})}$).

The time courses of the Ca^{2+} currents differed substantially for AMPAR and NMDAR channels (Fig. 7*c,d*). AMPAR channels activate rapidly but because the AP almost coincides with the peak conductance change, the Ca^{2+} current is strongly reduced during the AP because of the decreased driving force. In contrast, NMDAR channels activate more slowly, with most of the Ca^{2+} influx occurring after the AP. Notably, when based on the measured $I-V$ relationship (Fig. 6), the simulated Ca^{2+} current integral through NMDAR channels was approximately two times larger than the measured NMDAR-mediated influx of $\sim 0.8 \text{ pC}$. This could be attributable to the fact that EPSCs and Ca^{2+} fluxes were measured in different subsets of neurons; furthermore, a Ca^{2+} -dependent inactivation of NMDAR channels mediated by AMPAR or VDCC activation could contribute to the reduced Ca^{2+} influx during APs. Therefore, the NMDAR-mediated

Ca^{2+} current trace shown in Figure 7, *c* and *d*, was calculated with the Ca^{2+} $I-V$ relationship of Figure 6*c* but scaled by a factor of 0.44 to match the measured and simulated Ca^{2+} charge through NMDAR channels. With these assumptions, during the first 5 msec of the EPSP, the accumulations of Ca^{2+} in the postsynaptic cell through AMPAR and NMDAR channels were comparable (Fig. 7*e,f*). Interestingly, the NMDAR-mediated Ca^{2+} influx during this interval, which includes the rapid relief of NMDAR channels from the Mg^{2+} block during the AP, accounted for $<10\%$ of the total NMDAR-mediated Ca^{2+} influx. Most Ca^{2+} that flow into the cell via NMDAR channels enter during the depolarizing afterpotential, because the NMDAR channel conductance peaks ~ 10 msec after the presynaptic AP, and the depolarizing afterpotential increases the NMDAR-mediated Ca^{2+} charge by 20%, because it partially relieves the Mg^{2+} block of the NMDAR channels.

Differential localization of Ca^{2+} entry through NMDAR channels and VDCCs

Because of the large size of the axosomatic MNTB synapse, it was possible to resolve where Ca^{2+} entered through NMDAR channels and VDCCs. Simultaneous presynaptic and postsynaptic recordings were made, and the terminal and principal neuron each were filled with a different fluorescent dye to correlate postsynaptic Ca^{2+} changes with the location of the presynaptic terminal (Fig. 8*a*). Glutamate release was evoked by either a presynaptic voltage step ($n = 3$) or afferent stimulation ($n = 5$). In each of these experiments, presynaptic stimulation resulted in synaptic currents and fluorescence increases of the low-affinity dye OGB-5N in the postsynaptic cell. These fluorescence changes occurred first in close proximity to the presynaptic calyx and subsequently (within ~ 200 msec) spread over the entire postsynaptic neuron, although diffusion apparently was slowed by the nucleus (Fig. 8*b*). In the same experiments, Ca^{2+} influx through VDCCs was evoked by postsynaptic depolarizations, after blocking Na^+ and K^+ currents (Fig. 8*c*). In four experiments, the highest increases of fluorescence in the images taken 50 msec after this stimulation were observed in the region not covered by the terminal (114–147% compared with the region proximal to the terminal). In two experiments, the fluorescence increases opposite to the terminal were smaller than those in the region proximal to the terminal (61 and 88%). In two neurons, the fluorescence increases of the two regions differed by $<5\%$. The experiment in which the difference between the Ca^{2+} influx via NMDAR channels and VDCCs was largest is shown in Figure 8. In each of the four MNTB neurons in which the initial axon was visible in the fluorescence image, clear fluorescence increases in the axons were resolved (Fig. 8*c*), indicating the presence of VDCCs in the proximal axon. These results demonstrate that activation of the two main pathways of postsynaptic Ca^{2+} influx produces spatially different patterns of Ca^{2+} accumulation.

DISCUSSION

The results provide a quantitative description of the postsynaptic Ca^{2+} influx during synaptic transmission at the calyx-type synapse in the MNTB. A single presynaptic AP evoked in the postsynaptic neuron an EPSP that initiated a single AP. It caused, on average, a Ca^{2+} influx of 3 pC into the postsynaptic cell. A large fraction of the Ca^{2+} influx ($\sim 70\%$) was mediated by VDCCs, whereas the remaining charge was contributed by Ca^{2+} influx through GluR channels. The influx of Ca^{2+} via GluR

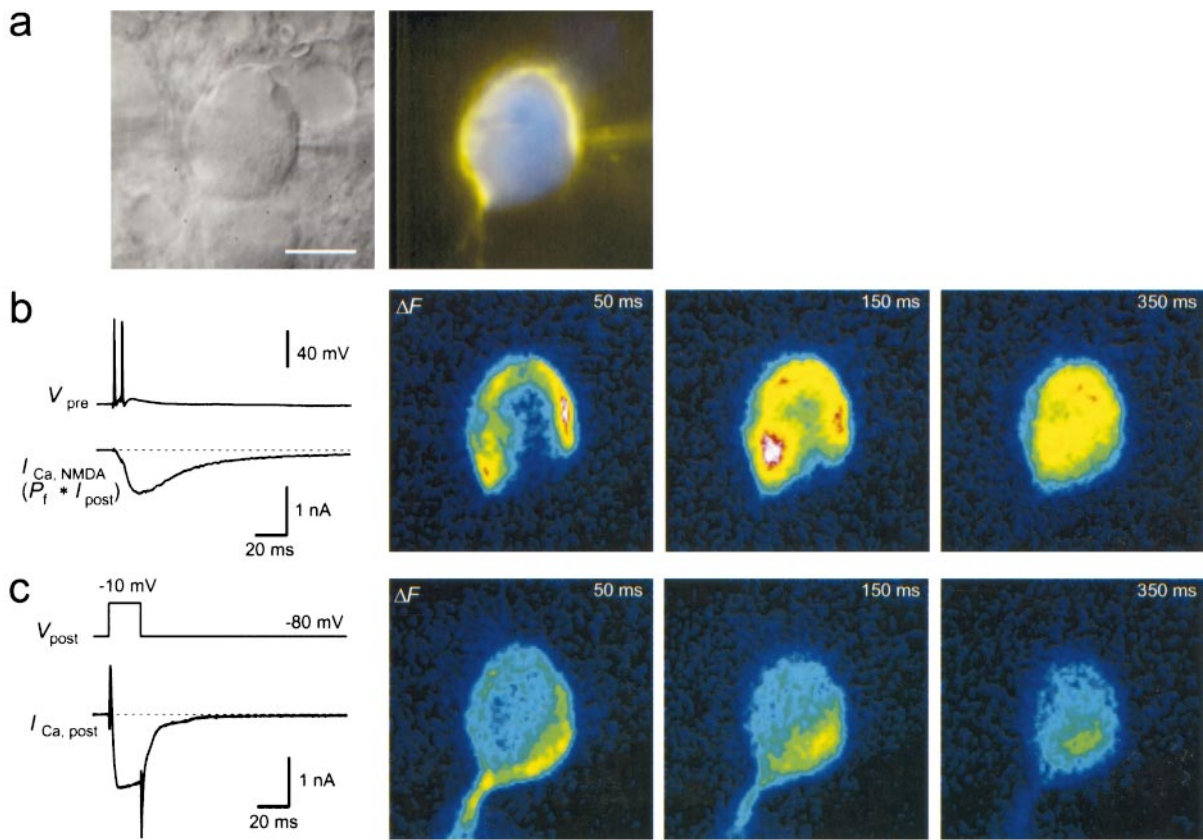


Figure 8. Localization of postsynaptic Ca^{2+} entry through NMDAR channels and VDCCs. *a*, Infrared video image (left) of an MNTB synapse from which a simultaneous presynaptic and postsynaptic recording was done. The presynaptic terminal was loaded with MagFura-2 (0.4 mM) by the pipette on the right, and the postsynaptic neuron was loaded with OGB-5N (0.4 mM). The right image shows the overlay of the presynaptic and postsynaptic fluorescence images (MagFura-2 pseudocolor code, yellow; OGB-5N pseudocolor code, blue). Scale bar, 10 μm . *b*, Two presynaptic APs (V_{pre}) elicited by afferent stimulation evoked a large NMDAR-mediated postsynaptic current at the synapse shown in *a* at a holding potential of -80 mV in Mg^{2+} -free extracellular solution. The estimated Ca^{2+} current through NMDAR channels is shown below, assuming a P_f of 11.6% ($I_{\text{Ca},\text{NMDA}}$). AMPARs were blocked by 10 μM NBQX. The average prestimulus fluorescence image was subtracted to obtain difference images (ΔF , right images), which represent the postsynaptic fluorescence changes of OGB-5N. ΔF images are shown at ~ 50 , 150, and 350 msec after afferent stimulation, at times when the total accumulated Ca^{2+} charge was 24, 44, and 55 pC, respectively. White corresponds to the largest fluorescence change. *c*, In the same MNTB neuron as shown in *a* and *b*, voltage steps from -80 to -10 mV (V_{post}) evoked a large inward Ca^{2+} current ($I_{\text{Ca},\text{post}}$) in the presence of TTX and TEA to block Na^+ and K^+ currents. On the right, OGB-5N difference images (ΔF) after subtraction of the prestimulus image are shown at ~ 50 , 150, and 350 msec after stimulation. Total accumulated Ca^{2+} charge was $\sim 40\text{ pC}$.

channels was dominated by the NMDAR channels, whereas AMPAR channels contributed <5% to the total Ca^{2+} influx. The NMDAR channels transported Ca^{2+} primarily subsynaptically, whereas the Ca^{2+} influx through VDCCs occurred more homogeneously throughout the plasma membrane of the cell body.

Dissection of different pathways for postsynaptic Ca^{2+} influx

The relative contribution of GluR channels and VDCCs to the postsynaptic Ca^{2+} influx was assessed by comparing Ca^{2+} influx during synaptically evoked APs, with the Ca^{2+} influx evoked by injecting current waveforms to mimic the shape of the synaptically evoked APs. The associated Ca^{2+} influx was measured using the fura-2 overload technique. Loading the postsynaptic neuron with 1 mM fura-2 was sufficient to outcompete the endogenous Ca^{2+} buffers, because their Ca^{2+} -binding ratio was ~ 90 , which is about twice the value found in the presynaptic terminal of the same synapse (Helmchen et al., 1997). In the presence of 1 mM fura-2, the Ca^{2+} transients decayed with time constants of several seconds (Fig. 1*d*, right). Therefore, postsynaptic Ca^{2+} clearance mechanisms were neglected during the first 0.5 sec after the AP. During overload conditions, Ca^{2+} influx of $\sim 10\text{ pC}$ led to bulk

cytoplasmic $[\text{Ca}^{2+}]_i$ increases of $<10\text{ nM}$. Under these conditions, Ca^{2+} -induced Ca^{2+} release (Eilers and Konnerth, 1997) is unlikely to occur. Other modes of Ca^{2+} release from internal stores are not likely to contribute either, because the relationship between the amount of Ca^{2+} entering the soma and the amplitude of fluorescence decrements was linear for a given fura-2 concentration and because Ca^{2+} transients measured at low fura-2 concentrations decayed monoexponentially.

When postsynaptic Ca^{2+} fluxes during current injection and afferent stimulation were compared, it was assumed that the properties of the VDCCs were not changed by the synaptically released glutamate. This assumption is reasonable, because inhibition of VDCCs by postsynaptic metabotropic GluRs is most likely too slow to modulate VDCCs during a single AP (Swartz and Bean, 1992).

Contribution of voltage-dependent Ca^{2+} channels

VDCCs contributed $\sim 2\text{ pC}$ of Ca^{2+} during a suprathreshold EPSP. This is about twofold higher than the Ca^{2+} influx into presynaptic terminals in the MNTB during a single AP (Borst and Sakmann, 1996; Helmchen et al., 1997). This difference in Ca^{2+} influx is probably because of the slower time course of the

postsynaptic APs. During APs, the Ca^{2+} current through VDCCs occurred during the repolarization phase of the AP (data not shown). This Ca^{2+} charge transport corresponds to a peak current of 1–2 nA through high-threshold VDCCs, which is a brief Ca^{2+} pulse 50–100 times larger than the GluR-mediated Ca^{2+} current at that instant. It might seem that the large relative contribution of the VDCCs could be a property characteristic for the giant MNTB synapse. However, a significant contribution of VDCCs to Ca^{2+} transients evoked by synaptic activation has also been reported for the dendrites of neurons, both under subthreshold conditions (Miyakawa et al., 1992; Markram and Sakmann, 1994) and under conditions when backpropagating APs open high-threshold VDCCs (Jaffe et al., 1992; Miyakawa et al., 1992). Furthermore, there is direct evidence for the presence of VDCCs in dendritic spines (Denk et al., 1996; Koester and Sakmann, 1998), and recently it was shown that during subthreshold activation ~80% of the Ca^{2+} influx into spines enters via VDCCs (Schiller et al., 1998).

Ca^{2+} influx through GluR channels

Previously, P_f values for NMDAR channels were determined by iontophoretic application or bath perfusion of GluR agonists (Schneggenburger et al., 1993; Burnashev et al., 1995; Neher, 1995). As shown in the present study, synaptically activated somatic NMDAR channels have a P_f of ~11–12%, similar to dendritic NMDAR channels in hippocampal CA1 pyramidal neurons (Garaschuk et al., 1996). For AMPAR channels, we determined a P_f of 1.1–1.5%. The observed NBQX- and d-APV-resistant current might reflect an incomplete block of NMDAR or AMPAR channels or a sustained activity of electrogenic glutamate transporters in the postsynaptic membrane (Otis et al., 1997). Previously measured P_f values for AMPAR channels range from 0.5 to 3.9% (Burnashev et al., 1995; Neher, 1995). Thus, the synaptic AMPAR channels in the MNTB have an intermediate P_f . This is consistent with the intermediate value for MNTB neurons of measured Ca^{2+} permeabilities of extrasynaptic AMPARs and the intermediate levels of mRNA encoding the GluR-B subunit (Geiger et al., 1995).

Direct and indirect contribution of GluR channels to Ca^{2+} influx

Remarkably, NMDAR channel activation accounted for as much as 30% of the total postsynaptic Ca^{2+} influx, and most of the Ca^{2+} entered directly via NMDAR channels. The time course of simulated NMDAR-mediated Ca^{2+} influx suggested that the relief of NMDAR channels from Mg^{2+} block during the overshoot of the AP only marginally enhanced Ca^{2+} influx through NMDAR channels (Fig. 7d). This is because NMDAR channels open predominantly after the AP, during the depolarizing afterpotential. The size of this afterpotential was clearly reduced in the presence of d-APV. The partial relief of the Mg^{2+} block caused by this d-APV-sensitive component of the afterpotential increased the Ca^{2+} influx via NMDAR channels by 20%. A similar mechanism is probably effective during subthreshold EPSPs at other synapses.

The P_f for AMPAR channels combined with the average charge of AMPAR-mediated EPSCs suggested that AMPAR channels contribute a surprisingly small percentage (<5%) to the total Ca^{2+} influx, primarily during the first 5 msec of an EPSP. This initial Ca^{2+} pulse could reduce the NMDAR channel opening by Ca^{2+} -dependent inactivation (Legendre et al., 1993; Vyklicky, 1993; Kyrozis et al., 1995). The effect could partially explain the finding that the measured NMDAR-mediated Ca^{2+}

charge during a single synaptically evoked AP was <50% of the NMDAR-mediated Ca^{2+} charge calculated from the simulation.

Spatial distribution of Ca^{2+} influx through different pathways

Spatially resolved imaging of postsynaptic Ca^{2+} accumulations revealed differential distributions of Ca^{2+} entry through NMDAR channels and VDCCs (Fig. 8). As expected, directly after stimulation, the glutamate-evoked Ca^{2+} accumulation was largest in close proximity to the terminal. In contrast, the initial VDCC-mediated fluorescence changes were distributed more homogeneously in the postsynaptic neuron and the initial axon. The most likely cause for these differences is that glutamate primarily activated synaptic NMDARs, whereas the postsynaptic voltage steps evoked Ca^{2+} influx through VDCCs that were localized more homogeneously throughout the somatic cell membrane. Similarly, subthreshold synaptic activation in dendrites can lead to Ca^{2+} increases restricted to single dendritic spines, whereas activation of VDCCs by a backpropagating AP causes a widespread Ca^{2+} signal in all spines and the dendritic shaft (Yuste and Denk, 1995; Koester and Sakmann, 1998).

Correlating the spatial patterns of fluorescence changes during voltage steps with the distribution of VDCCs is difficult for several reasons. The experiments were not done with a confocal microscope, which would be required to completely separate the contribution from synaptic and nonsynaptic regions. Also, because the experiments were not done in overload conditions, intracellular differences with respect to Ca^{2+} clearance and buffering would have to be investigated in detail before fluorescence changes can be considered directly proportional to Ca^{2+} influx. Nevertheless, the different patterns cannot be explained by a depletion of Ca^{2+} in the synaptic cleft, because in most experiments the absolute fluorescence increases near the terminal were larger after NMDAR activation than after activation of VDCCs. In addition, the overall decay of the Ca^{2+} transients mediated by VDCCs was similar in synaptic and nonsynaptic regions, suggesting that major differences in clearance mechanisms were also not responsible for the observed regional difference. Therefore, inhomogeneities in the density of VDCCs may exist in the postsynaptic membrane, which underlie the observed nonuniform increases of fluorescence during VDCC activation.

Functional significance of different Ca^{2+} pathways

Intracellular Ca^{2+} can modulate channel properties and regulate gene expression. A large fraction of the postsynaptic Ca^{2+} influx in MNTB neurons depends on the activation of NMDAR channels at postnatal days 8–10, whereas in 3- to 5-week-old rats, the AMPA-type GluR antagonist CNQX almost completely blocks the EPSP in the MNTB (Banks and Smith, 1992). This suggests that the contribution of the NMDAR channels decreases during development. Thus, one function of NMDAR channels could be to provide a strong Ca^{2+} signal, which might be required for the synthesis of proteins stabilizing the developing synapse. The Ca^{2+} signal evoked by suprathreshold EPSPs is generated both subterminally and, because of the location of VDCC-mediated Ca^{2+} influx, near the nucleus, which is usually located eccentrically, opposite to the presynaptic calyx (J.G.G. Borst, unpublished observations). Because the thresholds for activating Ca^{2+} and Na^+ channels were comparable (~−50 and −40 mV, respectively) (data not shown), the large Ca^{2+} influx observed during synaptic transmission will only be present if EPSPs evoke an AP. Therefore, nuclear Ca^{2+} signals could depend on whether the EPSPs are suprathreshold.

The action of Ca^{2+} on gene expression depends on the route Ca^{2+} takes into a neuron (Gallin and Greenberg, 1995). Both the different locations of Ca^{2+} entry and the differences in time course of AMPAR-, NMDAR-, and VDCC-mediated Ca^{2+} influx could account for the pathway-sensitivity of second-messenger cascades. It would be interesting to investigate whether for the MNTB synapse differences in gene expression levels are controlled by the Ca^{2+} accumulations through NMDAR channels and VDCCs, respectively.

REFERENCES

- Banks MI, Smith PH (1992) Intracellular recordings from neurobiotin-labeled cells in brain slices of the rat medial nucleus of the trapezoid body. *J Neurosci* 12:2819–2837.
- Barnes-Davies M, Forsythe ID (1995) Pre- and postsynaptic glutamate receptors at a giant excitatory synapse in rat auditory brainstem slices. *J Physiol (Lond)* 488:387–406.
- Bito H, Deisseroth K, Tsien RW (1997) Ca^{2+} -dependent regulation in neuronal gene expression. *Curr Opin Neurobiol* 7:419–429.
- Bliss TVP, Collingridge GL (1993) A synaptic model of memory: long-term potentiation in the hippocampus. *Nature* 361:31–39.
- Borst JGG, Sakmann B (1996) Calcium influx and transmitter release in a fast CNS synapse. *Nature* 383:431–434.
- Borst JGG, Helmchen F, Sakmann B (1995) Pre- and postsynaptic whole-cell recordings in the medial nucleus of the trapezoid body of the rat. *J Physiol (Lond)* 489:825–840.
- Burnashev N (1996) Calcium permeability of glutamate-gated channels in the central nervous system. *Curr Opin Neurobiol* 6:311–317.
- Burnashev N, Zhou Z, Neher E, Sakmann B (1995) Fractional calcium currents through recombinant GluR channels of the NMDA, AMPA and kainate receptor subtypes. *J Physiol (Lond)* 485:403–418.
- Denk W, Yuste R, Svoboda K, Tank DW (1996) Imaging calcium dynamics in dendritic spines. *Curr Opin Neurobiol* 6:372–378.
- Eilers J, Konnerth A (1997) Dendritic signal integration. *Curr Opin Neurobiol* 7:385–390.
- Forsythe ID, Barnes-Davies M (1993) The binaural auditory pathway: excitatory amino acid receptors mediate dual timecourse excitatory postsynaptic currents in the rat medial nucleus of the trapezoid body. *Proc R Soc Lond B Biol Sci* 251:151–157.
- Gallin WJ, Greenberg ME (1995) Calcium regulation of gene expression in neurons: the mode of entry matters. *Curr Opin Neurobiol* 5:367–374.
- Garaschuk O, Schneggenburger R, Schirra C, Tempia F, Konnerth A (1996) Fractional Ca^{2+} currents through somatic and dendritic glutamate receptor channels of rat hippocampal CA1 pyramidal neurones. *J Physiol (Lond)* 491:757–772.
- Geiger JRP, Melcher T, Koh D-S, Sakmann B, Seeburg PH, Jonas P, Monyer H (1995) Relative abundance of subunit mRNAs determines gating and Ca^{2+} permeability of AMPA receptors in principal neurons and interneurons in rat CNS. *Neuron* 15:193–204.
- Guinan Jr JJ, Li RY-S (1990) Signal processing in brainstem auditory neurons which receive giant endings (calyces of Held) in the medial nucleus of the trapezoid body of the cat. *Hear Res* 49:321–334.
- Helfert RH, Aschoff A (1997) Superior olivary complex and nuclei of the lateral lemniscus. In: The central auditory system. (Ehret G, Romand R, eds), pp 193–258. New York: Oxford UP.
- Helmchen F, Borst JGG, Sakmann B (1997) Calcium dynamics associated with a single action potential in a CNS presynaptic terminal. *Biophys J* 72:1458–1471.
- Herrington J, Bookman RJ (1994) Pulse control version 4.0: IGOR XOPs for patch clamp data acquisition and capacitance measurements. Miami: University of Miami.
- Jaffe DB, Johnston D, Lasser-Ross N, Lisman JE, Miyakawa H, Ross WN (1992) The spread of Na^+ spikes determines the pattern of dendritic Ca^{2+} entry into hippocampal neurons. *Nature* 357:244–246.
- Katz B (1969) The release of neural transmitter substances: the Sherrington lectures. Springfield, IL: Thomas.
- Kennedy MB (1989) Regulation of neuronal function by calcium. *Trends Neurosci* 12:417–420.
- Koester HJ, Sakmann B (1998) Calcium dynamics in single spines during coincident pre- and postsynaptic activity depend on relative timing of back-propagating action potentials and subthreshold excitatory postsynaptic potentials. *Proc Natl Acad Sci USA* 95:9596–9601.
- Koh D-S, Geiger JRP, Jonas P, Sakmann B (1995a) Ca^{2+} -permeable AMPA and NMDA receptor channels in basket cells of rat hippocampal dentate gyrus. *J Physiol (Lond)* 485:383–402.
- Koh D-S, Burnashev N, Jonas P (1995b) Block of native Ca^{2+} -permeable AMPA receptors in rat brain by intracellular polyamines generates double rectification. *J Physiol (Lond)* 486:305–312.
- Kyrozis A, Goldstein PA, Heath MJS, MacDermott AB (1995) Calcium entry through a subpopulation of AMPA receptors desensitized neighbouring NMDA receptors in rat dorsal horn neurons. *J Physiol (Lond)* 485:373–381.
- Legendre P, Rosenmund C, Westbrook GL (1993) Inactivation of NMDA channels in cultured hippocampal neurons by intracellular calcium. *J Neurosci* 13:674–684.
- Magee JC, Christofi G, Miyakawa H, Christie B, Lasser-Ross N, Johnston D (1995) Subthreshold synaptic activation of voltage-gated Ca^{2+} channels mediates a localized Ca^{2+} influx into the dendrites of hippocampal pyramidal neurons. *J Neurophysiol* 74:1335–1342.
- Magistretti J, Mantegazza M, Guatteo E, Wanke E (1996) Action potentials recorded with patch clamp amplifiers: are they genuine? *Trends Neurosci* 19:530–534.
- Markram H, Sakmann B (1994) Calcium transients in dendrites of neocortical neurons evoked by single subthreshold excitatory postsynaptic potentials via low-voltage-activated calcium channels. *Proc Natl Acad Sci USA* 91:5207–5211.
- Miyakawa H, Ross WN, Jaffe D, Callaway JC, Lasser-Ross N, Lisman JE, Johnston D (1992) Synaptically activated increases in Ca^{2+} concentration in hippocampal CA1 pyramidal cells are primarily due to voltage-gated Ca^{2+} channels. *Neuron* 9:1163–1173.
- Neher E (1995) The use of fura-2 for estimating Ca buffers and Ca fluxes. *Neuropharmacology* 34:1423–1442.
- Neher E, Augustine GJ (1992) Calcium gradients and buffers in bovine chromaffin cells. *J Physiol (Lond)* 450:273–301.
- Otis TS, Wu Y-C, Trussell LO (1996) Delayed clearance of transmitter and the role of glutamate transporters at synapses with multiple release sites. *J Neurosci* 16:1634–1644.
- Otis TS, Kavanaugh MP, Jahr CE (1997) Postsynaptic glutamate transport at the climbing fiber–Purkinje cell synapse. *Science* 277:1515–1518.
- Reyes AD, Rubel EW, Spain WJ (1996) *In vitro* analysis of optimal stimuli for phase-locking and time-delayed modulation of firing in avian nucleus laminaris neurons. *J Neurosci* 16:993–1007.
- Robinson HPC, Kawai N (1993) Injection of digitally synthesized synaptic conductance transients to measure the integrative properties of neurons. *J Neurosci Methods* 49:157–165.
- Schiller J, Schiller Y, Clapham DE (1998) NMDA receptors amplify calcium influx into dendritic spines during associative pre- and postsynaptic activation. *Nature Neurosci* 1:114–118.
- Schneggenburger R (1996) Simultaneous measurement of Ca^{2+} influx and reversal potentials in recombinant *N*-methyl-D-aspartate receptor channels. *Biophys J* 70:2165–2174.
- Schneggenburger R, Zhou Z, Konnerth A, Neher E (1993) Fractional contribution of calcium to the cation current through glutamate receptor channels. *Neuron* 11:133–143.
- Sharp AA, O’Neil MB, Abbott LF, Marder E (1993) The dynamic clamp: artificial conductances in biological neurons. *Trends Neurosci* 16:389–394.
- Spruston N, Jonas P, Sakmann B (1995) Dendritic glutamate receptor channels in rat hippocampal CA3 and CA1 pyramidal neurons. *J Physiol (Lond)* 482:325–352.
- Swartz KJ, Bean BP (1992) Inhibition of calcium channels in rat CA3 pyramidal neurons by a metabotropic glutamate receptor. *J Neurosci* 12:4358–4371.
- Vyklicky Jr L (1993) Calcium-mediated modulation of *N*-methyl-D-aspartate (NMDA) responses in cultured rat hippocampal neurones. *J Physiol (Lond)* 470:575–600.
- Wilcox KS, Fitzsimonds RM, Johnson B, Dichter MA (1996) Glycine regulation of synaptic NMDA receptors in hippocampal neurons. *J Neurophysiol* 76:3415–3424.
- Woodhull AM (1973) Ionic blockage of sodium channels in nerve. *J Gen Physiol* 61:687–708.
- Wu L-G, Borst JGG, Sakmann B (1998) R-type Ca^{2+} currents evoke transmitter release at a rat central synapse. *Proc Natl Acad Sci USA* 95:4720–4725.
- Yuste R, Denk W (1995) Dendritic spines as basic functional units of neuronal integration. *Nature* 375:682–684.
- Zucker RS (1994) Calcium and short-term synaptic plasticity. *Neth J Zool* 44:495–512.